Applied Catalysis B: Environmental 246 (2019) 266–276

Contents lists available at ScienceDirect

Applied Catalysis B: Environmental

journal homepage: www.elsevier.com/locate/apcatb

Effect of Cu doping on the anatase-to-rutile phase transition in TiO_2 photocatalysts: Theory and experiments

Ciara Byrne[a,b], Lorraine Moran[c], Daphne Hermosilla[d], Noemí Merayo[e], Ángeles Blanco[e], Stephen Rhatigan[f], Steven Hinder[g], Priyanka Ganguly[a,b], Michael Nolan[f,**], Suresh C. Pillai[a,b,*]

[a] Nanotechnology and Bio-Engineering Research Group, Department of Environmental Science, Institute of Technology Sligo, Ash Lane, Sligo, F91 YW50, Ireland
[b] Centre for Precision Engineering, Materials and Manufacturing Research (PEM), Institute of Technology Sligo, Ash Lane, Sligo, F91 YW50, Ireland
[c] Department of Life Sciences, Institute of Technology Sligo Ash Lane, Sligo, F91 YW50, Ireland
[d] University of Valladolid, E.U. Ingenierías Agrarias de Soria, Campus Duques de Soria, 42005 Soria, Spain
[e] Complutense University of Madrid, FCC Químicas, Ciudad Universitaria s/n, 28040 Madrid, Spain
[f] Tyndall National Institute, University College Cork, Lee Maltings, Dyke Parade, Cork, T12 R5CP, Ireland
[g] The Surface Analysis Laboratory, Faculty of Engineering and Physical Sciences, University of Surrey, Guildford, Surrey, GU2 7XH, United Kingdom

ARTICLE INFO

Keywords:
TiO_2
Doping
DFT
Oxygen vacancy
Photocatalysis

ABSTRACT

This paper shows that incorporation of Cu inhibits the anatase to rutile phase transition at temperatures above 500 °C. The control sample, with 0% Cu contained 34.3% anatase at 600 °C and transitioned to 100% rutile by 650 °C. All copper doped samples maintained 100% anatase up to 600 °C. With 2% Cu doping, anatase fully transformed to rutile at 650 °C, at higher Cu contents of 4% & 8% mixed phased samples, with 27.3% anatase and 74.3% anatase respectively, are present at 650 °C. All samples had fully transformed to rutile by 700 °C. 0%, 4% and 8% Cu were evaluated for photocatalytic degradation of 1, 4 dioxane. Without any catalyst, 15.8% of the 1,4 dioxane degraded upon irradiation with light for 4 h. Cu doped TiO_2 shows poor photocatalytic degradation ability compared to the control samples. Density functional theory (DFT) studies of Cu-doped rutile and anatase show formation of charge compensating oxygen vacancies and a Cu^{2+} oxidation state. Reduction of Cu^{2+} to Cu^{+} and Ti^{4+} to Ti^{3+} was detected by XPS after being calcined to 650–700 °C. This reduction was also shown in DFT studies. Cu 3d states are present in the valence to conduction band energy gap upon doping. We suggest that the poor photocatalytic activity of Cu-doped TiO_2, despite the high anatase content, arises from the charge recombination at defect sites that result from incorporation of copper into TiO_2.

1. Introduction

Titanium dioxide (TiO_2) was first commercially used during the 20th century for applications that include pigments in paint, UV blockers, batteries and food colouring. Since 1972, when Fujishima and Honda first reported the splitting of water using TiO_2, [1] its use as a photocatalyst has gained significant interest [2–4]. There are numerous reasons why TiO_2 remains the most researched photocatalyst. These include ease of preparation, strong oxidising ability, long term stability, nontoxicity, high refractive index, high dielectric constant and low cost [5,6]. The potential for use of TiO_2 in energy and environmental applications is another reason why TiO_2 continues to be examined. Of particular importance are hydrogen production, CO_2 reduction, solar cells, self-cleaning coatings and degradation of organic compounds (e.g. phenol) in water [6–9]. The large band gap (3.2 eV for anatase) is partly responsible for its use as a photocatalyst [10]. The band gap has a direct impact on the rate of electron-hole recombination during photocatalysis and titania has a relatively slow recombination rate compared to most photocatalysts [5].

TiO_2 is naturally present in three main phases: anatase (tetragonal, a = b = 3.785 Å, c = 9.54 Å), brookite (orthorhombic, a = 5.143 Å, b = 5.456 Å, c = 9.182 Å) and rutile (a = b = 4.593 Å, c = 2.959 Å) [11,12]. The thermodynamically metastable phases, anatase and brookite, transition irrevocably into the stable rutile phase at high temperatures [5]. Generally this takes place in the range of 600–700 °C in pure synthetic TiO_2. Of these TiO_2 phases, anatase is considered to be the most photocatalytically active phase. It can however only be activated by UV light, which accounts for *ca.* only 4% of the solar spectrum

* Corresponding author at: Nanotechnology and Bio-Engineering Research Group, Department of Environmental Science, Institute of Technology Sligo, Ash Lane, Sligo, F91 YW50, Ireland.
** Corresponding author.
E-mail addresses: michael.nolan@tyndall.ie (M. Nolan), pillai.suresh@itsligo.ie (S.C. Pillai).

https://doi.org/10.1016/j.apcatb.2019.01.058
Received 27 September 2018; Received in revised form 19 December 2018; Accepted 20 January 2019
Available online 22 January 2019
0926-3373/

[9]. In order to stabilise the anatase phase at elevated temperatures and to utilise UV and visible light for photocatalysis, chemical modifiers and dopants can be used. These include anion dopants, e.g. carbon [13,14], and nitrogen [15,16], or metal dopants, e.g. iron [17,18], and silver [19,20].

Copper has been previously investigated as a potential dopant in TiO_2 [9,21–28] but to date a detailed systematic analysis of the effect of Cu doping on the phase stability of TiO_2 is lacking [29]. In an important contribution, Yoong et al. examined Cu-doped Degussa P25 TiO_2 for different weight% of Cu (0, 2, 5, 10, 15%) at three temperatures (300, 400, 500 °C) [29]. However, the highest temperature in this work is below the anatase-rutile phase transition [10]. Hence there is no comprehensive understanding of the effect of copper doping on the anatase-rutile phase transition in TiO_2. Unravelling the role of Cu in this phase transition will clearly be beneficial in stabilising the more photoactive anatase phase of TiO_2 at higher temperatures.

Therefore, the aim of this investigation was to carry out a systematic and detailed study of the impact of copper doping of titanium dioxide on the anatase content, having calcined the samples to temperatures in the range 400–800 °C. Having determined the crystalline composition of the samples we examine the resulting photocatalytic activity. We have prepared copper doped titania with four different Cu concentrations, namely 0, 2, 4 and 8 mol. % Cu and these were calcined between 400–800 °C. Density functional theory (DFT) studies of Cu doping of bulk rutile and anatase were carried out to explore the effect of doping on the cation oxidation states, oxygen vacancy formation and any changes to the electronic structure of rutile and anatase after doping. X-ray diffraction (XRD) analysis and Raman spectroscopy were used for determining the phase composition of each sample. X-ray photoelectron spectroscopy (XPS) was used for identifying the bonding that was present in samples.

2. Materials & methods

2.1. Chemicals & reagents

Titanium tetraisopropoxide (97%), copper sulphate pentahydrate (≥98.0%) and isopropanol (≥99.5%) were purchased from Sigma-Aldrich and were used without further treatment. 1,4-dioxane was purchased from Merck.

2.2. Preparation of nanomaterials

2.2.1. Preparation of TiO_2

46.16 mL of titanium isopropoxide (TTIP) was added to 200 mL of isopropanol (IPA). This solution was stirred for 15 min. To this solution 200 mL of deionised water was added. This mixture was stirred for another 30 min. The resulting gel was dried in the oven set at 100 °C for 12 h. The resulting powder was annealed at 400 °C, 500 °C, 600 °C, 650 °C, 700 °C and 800 °C, at a ramp rate of 10 °C/min and held at the target temperature for 2 h.

2.2.2. Preparation of copper doped materials

For a 2% copper sample, 45.24 mL of TTIP was added to 200 mL of IPA and was stirred for 15 min (Solution A). 0.8705 g of copper sulphate ($CuSO_4$) was added to 200 mL of deionised water, this was stirred for 15 min (Solution B). Solution B was added to Solution A and this was stirred for 30 min. The resulting gel was dried in the oven at 100 °C for 12 h. The resulting powder was annealed at 400 °C, 500 °C, 600 °C, 650 °C, 700 °C and 800 °C, at a ramp rate of 10 °C/min and was held for 2 h. This method was repeated for the 4% and 8% copper samples by altering the amount of TTIP and $CuSO_4$ (4%–44.32 mL and 1.7375 g; 8%–42.47 mL and 3.5075 g).

2.3. Characterisation

All samples were analysed with X-ray Diffraction (XRD). The diffractograms were produced using a Siemens D500 X-ray powder diffractometer, using Cu Kα radiation (λ = 0.15418 nm). The diffraction range examined was between 2θ = 10°–80°. To determine the fraction of rutile in the samples, the Spurr equation was used (Eq. (1)) [30].

$$F_R = \frac{1}{1 + 0.8\left[\frac{I_A(101)}{I_R(110)}\right]} \quad (1)$$

where F_R is the quantity of rutile in mixed sample and $I_A(101)$ and $I_R(110)$ are the intensities of the main anatase and rutile peaks.

The crystallinity of the samples were calculated using the XRD spectra and the Scherrer equation (Eq. (2)) [31].

$$\Phi = \frac{K\lambda}{\beta \cos\theta} \quad (2)$$

where Φ is the crystallite size, K is the shape factor, λ is the X-ray wavelength, β is the full line width at the half-maximum height of the main intensity peak and θ is the Bragg angle.

The Horiba Jobin Yvan LabRAM HR 800 with a grating of 300gr/mm was used for Raman analysis. A 660 nm solid state diode laser standard bandwidth version with double edge filter upgrade was the laser used. The acquisition time was 3 s. When focusing onto the sample a X50 lens was used.

A ThermoFisher Scientific Instruments (East Grinstead, UK) K-Alpha$^+$ spectrometer was utilised in obtaining XPS spectra, with a monochromated Al Kα X-ray source ($h\nu$ = 1486.6 eV) and ~400 µm radius was used as an x-ray spot. The survey spectra and a high-resolution core level spectrum for all elements was obtained using a Pass Energy of 200 eV and 50 eV, respectively. The C1s peak (285) was used as a charge reference to account for charging effects during acquisition. The non-linear (Shirley) background was removed from the high resolution, core level spectra before calculating the quantitative surface chemical analyses. The manufacturers Avantage software was used which incorporates the appropriate sensitivity factors and corrects for the electron energy analyser transmission function.

The surface morphology of the samples was analysed using the Siemens TM1000 Scanning Electron Microscopy with Energy Dispersive X-Ray Analyser (SEM-EDX).

In order to determine the surface area of the samples the Brunauer–Emmett–Teller method (BET) was used. The samples were first degassed for an hour at 300 °C. The adsorption isotherms were acquired at −196.15 °C.

The following analyses were made according to the standard methods for the examination of water and wastewater (APHA 2005). Total organic carbon (TOC) was measured by the combustion-infrared method using a multi N/C® 3100 TOC/TN analyser (Analytik Jena AG, Jena, Germany), which performed the catalytic combustion on cerium oxide at 850 °C.

1,4-Dioxane was quantified using gas–liquid chromatography (GLC) on a 7980 A instrument (Agilent Technologies Inc., Palo Alto, CA) equipped with a flame ionization detector. The temperatures of the injector and the detector were 310 °C and 280 °C, respectively. Samples (2 µL) were injected using the pulsed-split mode (split ratio 5:1) and analysed in a TRB-FFAP (Teknokroma, Sant Cugat del Vallès, Spain) fused silica column (30 m x 0.25 mm internal diameter × 0.25 µm film thickness) with He (43 psi) as carrier gas, and the following temperature programme: 80 °C to 240 °C at a 15 °C/min ramp rate, after a 9 min initial hold. Peaks were identified according to relative retention time figures provided by commercial standards. Quantification was performed according to peak area, corrected with the response factors calculated for each compound using 1-butanol (60 ppm) as internal standard, and the GC-ChemStation software Rev.B.04.02 (96) from Agilent.

2.4. Photocatalysis

Experiments were performed with a synthetic solution of 1,4-dioxane (75 mg/L) that was kept stirred during the experiment using a magnetic device. The corresponding doped-TiO_2 catalyst was added to the suspension with a concentration of 1 g/L. The photocatalytic reaction was performed for duration of 240 min. Samples were withdrawn from the solution every 30 min. The source of UV light was a solar simulator supplied by Newport (Irvine, USA) equipped with a Xenon lamp (300 W). A correction filter (ASTM E490-73a) provides the simulated solar spectrum under ideal conditions. A total photon flux of $6.8{\cdot}10^{19}$ photon$\cdot s^{-1}$ was calculated to flow inside the photochemical reactor, as described by Liang et al. (2011). Light intensity between 200 to 400 nm resulted of 150 W$\cdot m^{-2}$ at 3 cm from the light source, which was the distance between the sample surface and the lamp. Light intensity was recorded using a radiometer (UV-Elektronik, UV-VIS Radiometer RM-21, Ettlingen, Germany).

The light intensity recorded on the irradiated liquid surface in W$\cdot m^{-2}$ (J$\cdot s^{-1}$ m^{-2}) was converted to kJ/L taking into account the volume of the solution (50 mL) and the irradiated surface (0.0104 cm^{-2}) in order to normalize the data. Blank experiments either performed without adding the catalyst, without switching the UV lamp on, or using no dopant concentration were performed. All experiments were repeated three times.

2.5. Density functional theory computations

Calculations were performed using the VASP5.2 [32,33] code with projector augmented wave [34,35] (PAW) potentials to account for the core-valence interaction and a kinetic energy cut-off of 400 eV. Ti is described with 12 valance electrons, Cu with 11 and O with 6. The bulk unit cell was optimised using standard DFT and for rutile, the optimised lattice parameters are a = 4.613 Å and c = 2.961 Å. For anatase, the optimised lattice parameters are a = 3.791 Å and c = 9.583 Å. Cu was substitutionally doped onto a Ti site in rutile (2 × 2 × 3) and anatase (2 × 2 × 2) supercells. This gives a dopant concentration of 3.1 at.% for rutile and anatase, which is consistent with experimental concentrations of Cu in TiO_2 [22,36,37]. The k-point sampling used a Monkhorst-Pack (4 × 4 × 2) grid for both bulk polymorphs. Structures were relaxed until forces were less than 0.01 eV $Å^{-1}$.

Calculations were performed taking into account spin polarisation and no symmetry constraints were imposed. In the DFT + U calculations, U = 4.5 eV was applied to the Ti 3d states and U = 7 eV was applied to the Cu 3d states, arising from the inability of DFT to describe consistently the Cu^{2+} oxidation state of Cu [38,39]. An additional U = 7 eV is applied to the O 2p states to described the localised oxygen polaron in the doped systems prior to the formation of a charge compensating oxygen vacancy. These choices for U are based on previous studies [40–44]. The starting geometries were manually distorted from the symmetric bulk geometry in order to examine relaxation to distorted geometries which can be compared with undistorted geometries. To study the charge compensation that arises as a result of the difference in the Cu^{2+} and Ti^{4+} oxidation states, one oxygen ion was removed from different sites of the most stable Cu-doped structures and the energy of formation was calculated via:

$$E^{vac} = E(Cu_xTi_{1-x}O_{2-y}) + 1/2E(O_2) - E(Cu_xTi_{1-x}O_2) \quad (3)$$

where $E(Cu_xTi_{1-x}O_{2-y})$ is the total energy of Cu doped TiO_2 with a charge compensating oxygen vacancy and $E(Cu_xTi_{1-x}O_2)$ is the total energy of Cu-doped TiO_2. The formation energy is referenced to half the total energy of O_2. A similar formula is used to compute the formation energy of the subsequent reducing oxygen vacancy.

Given that copper ions can take a 2+ oxidation state, these calculations were therefore performed with 1 and 3 unpaired spins which takes into account the electron deficit due to substitutional doping of Cu^{2+} for Ti^{4+} and the d^9 configuration of Cu^{2+}. The oxidation states of the Cu dopant and lattice Ti and O ions were determined from Bader charge analysis [45] and spin magnetisations and these values are quoted in the results.

3. Results and discussion

3.1. X-ray diffraction (XRD) characterisation

X-ray Diffraction (XRD) was used to determine the effect of copper on the anatase to rutile transition temperature in TiO_2. The intensities of the main anatase and rutile peaks (101 and 110 respectively) were used in the Spurr equation (Eq. (1)) for calculating the % anatase and % rutile present in each sample. There were no peaks present relating to copper metal (which appear at approx. 2θ = 43, 50 and 74°) [21], the only peaks that were present were those for titanium dioxide. The uncalcined samples are partially amorphous as all the peaks are not fully visible in the XRD (Fig. S1). All samples were 100% anatase phase at 400 °C and 500 °C. At 600 °C, the control (0%) was 34.3% anatase and 65.7% rutile while the copper doped samples remained 100% anatase (Fig. S2). At all temperatures above 650 °C, the 0% and 2% Cu-TiO_2 samples contained 100% rutile. However, at the same temperature the 4% and 8% Cu-TiO_2 had 27.3% anatase and 74.3% of anatase respectively (Fig. 1). All samples were 100% rutile phase at temperatures above 700 °C (Fig. S3). Fig. 2 shows the composition profile of the samples prepared.

XRD was also used to determine the crystallinity of all samples (Table 1) using the Scherrer equation (Eq. (2)). Generally as the temperature increases so does the crystallinity. The origin of this is due to the samples converting from the anatase phase (with a smaller crystalline size) to the rutile phase. At 400 °C, 500 °C and 600 °C all doped samples show a smaller crystalline size compared to the undoped sample, indicating that at these temperatures Cu doping stabilises the anatase phase. The 8% Cu sample has lowest crystalline size in the range of 400–700 °C,

3.2. Raman spectroscopy

The anatase to rutile transition of Cu-TiO_2 was further examined using Raman spectroscopy. A typical Raman spectrum shows characteristic modes at different wavenumbers corresponding to Raman shifts [10]. The active modes for anatase are *A1g*, *2B1g* and *3 Eg* at 147, 197, 396, 516 and 638 cm^{-1} [10]. For rutile the Raman active modes are *A1g, B1g, B2g* and *3 Eg* at 144, 238, 446, 612 and 827 cm^{-1} [10]. Raman spectra showed the presence of the titania peaks and did not show the occurrence of copper/copper oxides or other impurities. If we consider the example of 0% Cu-doping of TiO_2, then samples calcined at 500 °C exhibited 100% anatase phase (Fig. 3), while 0% Cu-TiO_2 calcined at 600 °C illustrated a mixed phase profile (Fig. 3). The peaks for

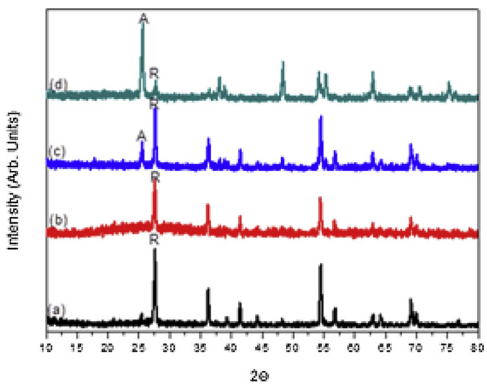

Fig. 1. XRD of (a) 0% Cu-TiO_2 (b) 2% Cu-TiO_2 (c) 4% Cu-TiO_2 (d) 8% Cu-TiO_2 after calcining to 650 °C A = anatase and R = Rutile.

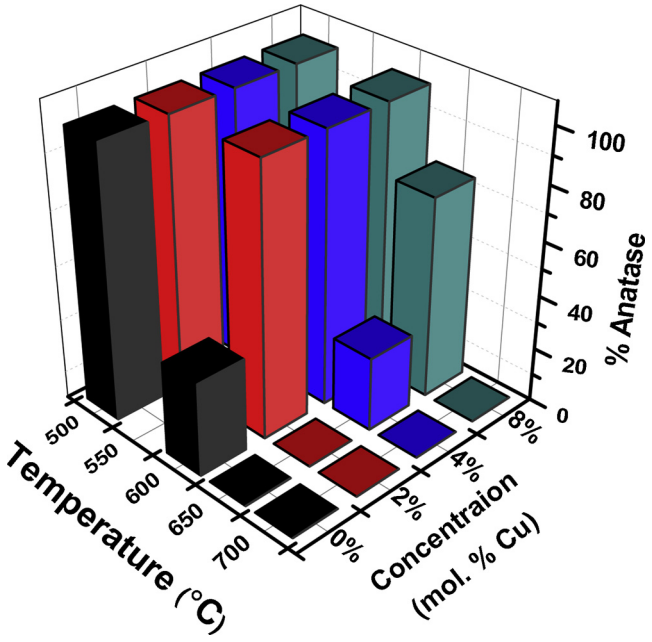

Fig. 2. Percentage of the anatase phase in Cu-doped TiO_2 samples.

Table 1
Crystalline size (in nm) of all samples calcined at 400 °C, 500 °C, 600 °C, 650 °C, 700 °C and 800 °C.

	0% Cu	2% Cu	4% Cu	8% Cu
400 °C	7.06	6.15	5.75	5.07
500 °C	10.11	8.98	6.77	5.49
600 °C	17.73 (A) 19.88 (R)	15.46	14.02	14.07
650 °C	24.87	25.03	23.65 (A) 26.14 (R)	21.10 (A) 22.70 (R)
700 °C	27.12	28.45	26.09	24.09
800 °C	33.94	31.36	29.20	25.18

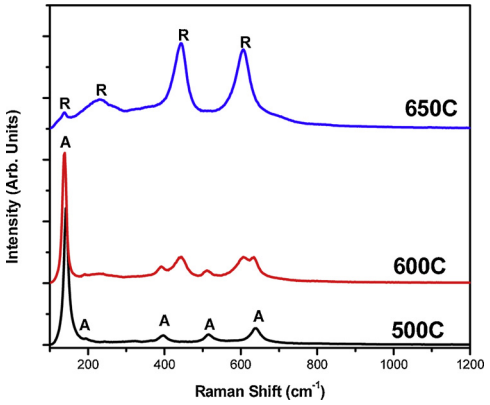

Fig. 3. Raman spectra of 0% Cu-doped TiO_2.

100% rutile phase can be observed for the 0% Cu-TiO_2 sample when calcined at 650 °C (Fig. 3). The Raman spectra of 8% Cu-TiO_2 are shown in Fig. S4. This figure shows that the 8% Cu-TiO_2 is anatase at 600 °C and rutile at 700 °C. However, in contrast to XRD, 8% Cu-TiO_2 at 650 °C appears to only show anatase peaks. This is due to the high % of anatase present (74.3%) and is a result of Raman spectroscopy being less sensitive than XRD.

3.3. X-ray photoelectron spectroscopy (XPS)

The X-ray Photoelectron spectroscopy (XPS) measurements were performed to analyse the elemental composition and metal oxidation states of each sample. XPS analysis was performed on all samples that were treated at 600 °C, 650 °C and 700 °C. Fig. 4(a) illustrates the survey spectrum for the example of samples with 8% Cu-doping and which were calcined at 600 °C, 650 °C and 700 °C. The survey spectrum indicates the presence of Titanium, Oxygen, Copper and Sulphur. C1s peaks (at binding energies (BE) of 284.9–285.0 eV) are present in all samples. These peaks can be attributed to adventitious carbon (C—C, C═C and/or C—H bonds) which arise due to contamination during synthesis and calcination [10,46]. The concentrations of the elements present in the Cu-doped TiO_2 materials are tabulated in Table S1. Sulphur is present at *ca.* 4 at.% in the 8% Cu material calcined at 600 °C, Table S1. The presence of sulphur in Cu-doped TiO_2 at this concentration is mostly likely due to the release of sulphur dioxide from the Cu precursor ($CuSO_4$) during the calcination process [47]. However, the amount of Sulphur reduces to below 1 at.% in the composites calcined at 700 °C (Table S1), which is also evident from the Sulphur 2p spectrum in Fig. 4(e).

The peaks for the Ti2p $_{3/2}$ spectrum show the presence of Ti—O binding. The slight decrease in the binding energy (464.6–464.4 eV) as the temperature increases is an indicator of samples becoming oxygen deficient, see Fig. 4(b) and Tables S2 and S3 [10,12]. This change is also an indication of Ti^{4+} reduction to Ti^{3+} at higher temperature [10,12]. There is a similar decrease in the binding energy of the O1s peak (BE = 530.4–530.1 eV), shown in Fig. 4(c) and Tables S2 and S3. This slight decrease in the O1s BE further indicates the formation of oxygen vacancies [12]. The formation of oxygen vacancies (as determined from the O1s and Ti2p $_{3/2}$ peaks) signifies that the anatase phase is beginning the transformation to the rutile phase [10,12,48]. The second dominant peak in the O1s spectra at 532.6 eV in Cu-TiO_2 calcined at 600 °C shows a shift to 531.7 eV, when calcined at 700 °C. These peaks are assigned to oxygen in the sulphate and oxygen bound to Cu (as Cu^{2+}) respectively [49].

As XPS is significantly more sensitive than XRD and Raman to minute compositional changes such changes can be detected from XPS analysis, i.e. any copper oxides that may form can be detected in XPS but not in XRD and Raman spectra [11]. Fig. 4(d) shows the Cu2p $_{3/2}$ spectra of 8% Cu-TiO_2 samples calcined at 600 °C, 650 °C and 700 °C. The sample calcined at 600 °C exhibits a broad asymmetric curve from 930 eV to 937 eV. The deconvolution of this curve gave 2 prominent peaks at 933.1 eV and 936 eV corresponding to Cu^{2+} in CuO and $CuSO_4$ respectively. Calcining at higher temperatures of 650 °C and 700 °C resulted in slight shift in these peaks. At 700 °C the peaks were observed at 932.6 eV and 934.1 eV corresponding to Cu^{1+} and Cu^{2+} oxidation states, respectively. Hence, XPS results revealed the presence of copper in two oxidation states. Moreover, two satellite peaks of Cu2p$_{3/2}$ that correspond to the Cu^{2+} oxidation state are observed at 941 eV and 944 eV; the peak intensities gradually decreased as the calcination temperature increased [10,50]. The S2p (Fig. 4(e)) XPS spectrum shows two sub-component peaks at 170.1 eV and 168.8 eV, these are attributed to S2p $_{1/2}$ and S2p $_{3/2}$ respectively and these binding energies suggest the presence of sulphur in S^{6+} state [10].

3.4. Effect of Cu doping and temperature on surface area

BET analysis was performed in order to determine the surface area and porosity of the sample. Table 2 shows the surface area and the porosity for the control (0% Cu) and the example of 8% Cu-TiO_2, which shows the highest anatase-rutile transition temperature. The surface area for the control is significantly smaller than that of the 8% copper sample calcined at 500 °C (both 100% anatase) and 600 °C (0 Cu % = 34.3% anatase; 8 Cu% = 100% anatase). After calcining at 700 °C (where both samples are 100% rutile) the two samples have similar

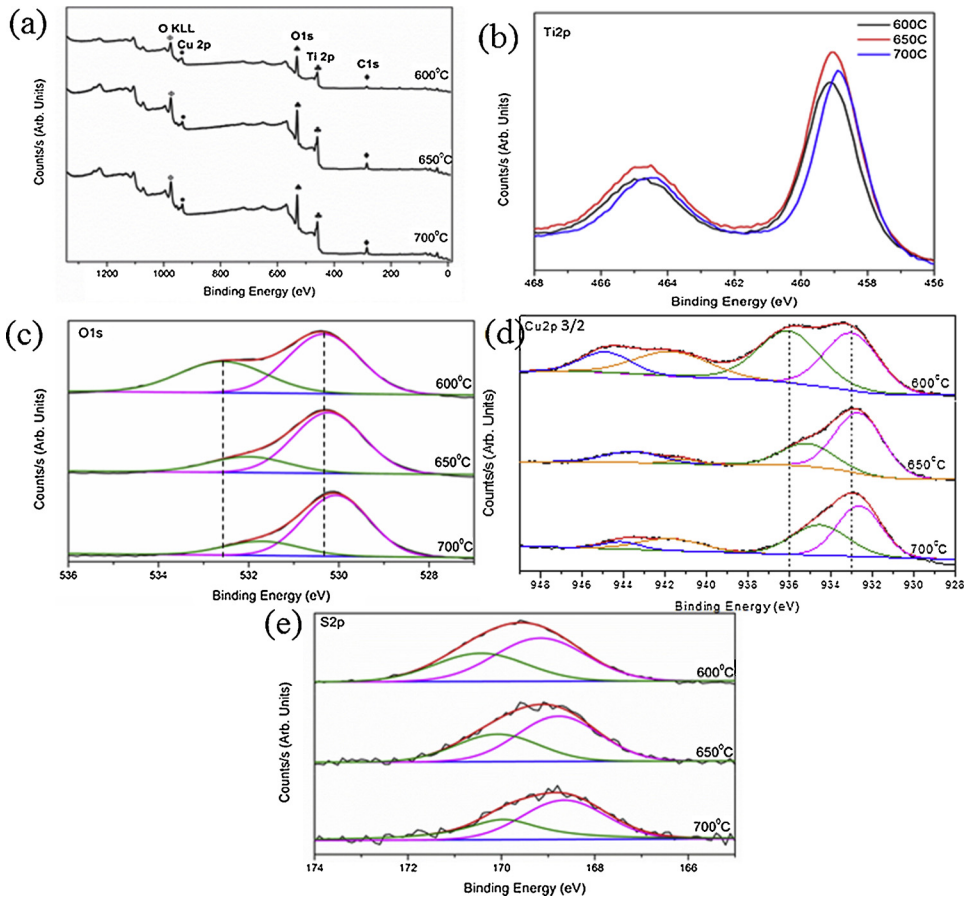

Fig. 4. XPS spectra for the example of 8% Cu-TiO_2 that was calcined at 600 °C, 650 °C and 700 °C, Part (a) shows the survey spectrum, (b) shows the Ti2p BE region, (c) shows the O1s BE region, (d) shows the Cu2p $_{3/2}$ BE region and (e) shows the S2p BE region.

Table 2
Surface area and porosity of 0% and 8% Cu-TiO_2 calcined at 500 °C, 600 °C & 700 °C.

Sample	Surface area (m^2/g)	Pore volume (Å)
0% Cu-TiO_2 500 °C	57.4	26.5
0% Cu-TiO_2 600 °C	6.6	26.5
0% Cu-TiO_2 700 °C	3.5	24.4
8% Cu-TiO_2 500 °C	83.2	27.8
8% Cu-TiO_2 600 °C	21.2	26.9
8% Cu-TiO_2 700 °C	3.9	26.7

surface areas. There are small differences in the pore volumes of the different samples. For example, in pure TiO_2 these range from 24 to 26 Å and for 8% Cu-TiO_2 these range from 26 to 27 Å (Table 2).

3.5. Scanning electron microscopy- energy dispersive X-ray analyser (SEM-EDX)

The morphology and elemental composition were examined using Scanning Electron Microscopy with an Energy Dispersive X-Ray Analyser (SEM-EDX). No specific shapes were able to be determined due to the agglomeration of the samples, as a result of the high calcination temperatures. Examples of SEM-EDX results are shown in the supplementary information (Figs. S5 & S6).

3.6. Density functional theory simulations

3.6.1. Atomic and electronic structure of Cu-doped TiO_2

The local atomic structure that results from substituting Cu on a Ti site in Cu-doped bulk rutile and anatase TiO_2 (see Fig. S7), is distorted about the dopant site. Replacing a Ti^{4+} cation with a Cu^{2+} cation results in a deficiency of two electrons and formation of two oxygen holes. Two energy minima are found. In the first, the local atomic structure is distorted symmetrically about the dopant with the distortion arising from differences in ionic radii between copper and titanium. The second is an asymmetric distortion to the geometry.

In the first solution the four-equatorial dopant-O distances are equal (1.96 Å (1.91 Å) for rutile (anatase)) as are the two apical dopant-O distances (1.97 Å (1.97 Å) for rutile (anatase)). In undoped rutile (anatase), the equatorial/apical Ti-O distances are 1.96/1.98 Å (1.93/2.01 Å). Upon doping, the equatorial and apical Cu-O distances are shorter than the equivalent Ti-O distances in undoped TiO_2. The symmetric structure is consistent with delocalisation of the oxygen holes and the results for rutile are similar to those previously reported [51]. Figs. 5(a) and (c) show that with DFT, the oxygen holes which form upon Cu doping are delocalised over all oxygen ions in rutile and more localised in anatase, but still notably delocalised.

The asymmetric solution, with a geometry distortion about the dopant, shows non-uniform dopant-O distances. For rutile, there is one elongated Cu—O distance, consistent with a longer bond between Cu and an oxygen hole polaron. This has also been observed in In-doped rutile TiO_2 [52] and Li-doped MgO [39] and ZnO [53] among other materials [38,54–56]. That the effect is less strong in Cu-doped TiO_2 can be attributed to the presence of a second hole which is less localised, being distributed over oxygen ions neighbouring the dopant, as shown by the spin density plot in Fig. 5(b). This diminishes the Coulombic attraction and lengthens the cation—O bonds. We find that a solution starting with two fully localised holes relaxes to the partially localised hole distribution just described.

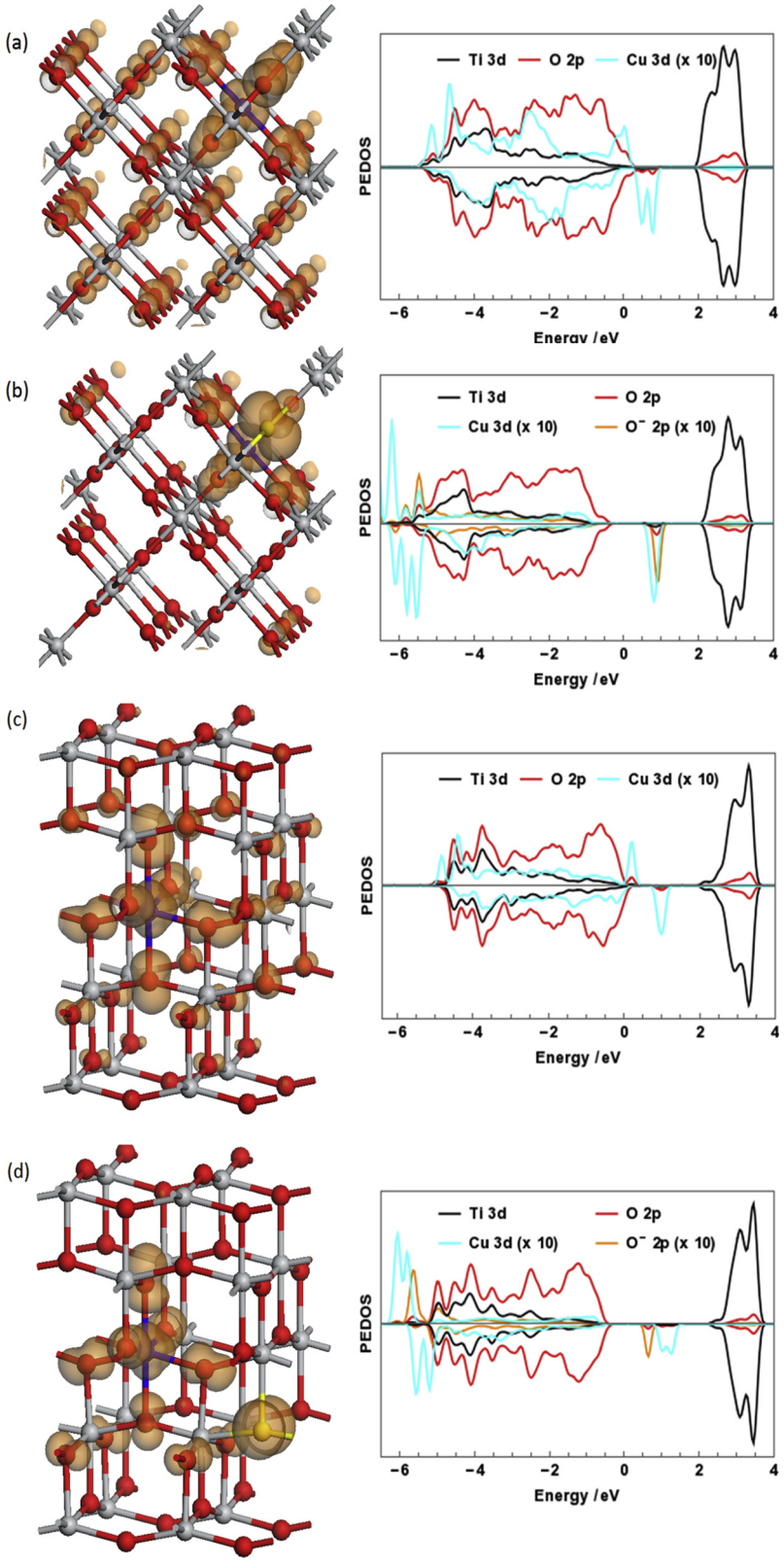

Fig. 5. Spin density and PEDOS plots for Cu-doped rutile TiO_2 for (a) DFT and (b) DFT + U and Cu-doped anatase TiO_2 for (c) DFT and (d) DFT + U. Cu is represented in blue with yellow marking the position of the oxygen polarons. The spin isosurfaces are set to 0.02 electrons $Å^{-1}$ (For interpretation of the references to colour in this figure legend, the reader is referred to the web version of this article).

In the case of anatase, the polaron is not bound directly to the dopant and sits at an equatorial site of a neighbouring Ti (yellow sphere in Fig. 5(d)). The polaron induces a significant extension of the Ti-O distance of between 0.07 and 0.1 Å when compared to undoped TiO_2. The second polaron is also partially localised over oxygen ions near the dopant.

The asymmetric polaronic solution is more stable by 0.2 eV in rutile and anatase, within the present DFT + U computational set-up. The

asymmetric solution is not stable with DFT, consistent with previous work showing that only symmetric solutions are stable with DFT [52].

The identity of the polaron is further confirmed through the calculated Bader atomic charges and the spin magnetisations. For a polaronic oxygen the computed Bader charge is reduced from 7.4 electrons (lattice O^{2-}) to 6.7 (6.9) electrons for Cu-doped rutile (anatase). The calculated spin magnetisations are 0.85 (0.71) μ_B in rutile (anatase). In rutile, the other five oxygen ions neighbouring the dopant have spin magnetisations in the range of 0.16 to 0.22 μ_B. Similarly, in anatase, five of the six oxygen ions neighbouring the dopant have spin magnetisations in the range of 0.12 to 0.17 μ_B, with a value of 0.33 μ_B on a sixth oxygen, namely lower apical oxygen bonded to the dopant in Fig. 5(d). The Bader charges of the Cu dopant are 9.6 electrons for rutile and 9.7 electrons for anatase, consistent with the Cu^{2+} oxidation state [57].

Fig. 5(b) and (d) display the projected electronic density of states (PEDOS), projected onto the Ti and Cu 3d states and the O 2p states. The PEDOS plots show qualitatively similar behaviour for both doped phases. The DFT calculations, with the delocalised symmetric solution, have states associated with the oxygen holes positioned just above the valence band, crossing the Fermi level. For anatase, in which the polaron is partially localised over oxygen ions near the dopant, even without the + U correction, an O 2p state appears in the gap, just above the VB. These results concur with previous *ab initio* studies of rutile [51] and anatase [58].

Applying the + U correction to the O 2p, Ti 3d and Cu 3d states, proved necessary to obtain a properly localised polaron description [38,39,54] and the PEDOS plots consequently display the typical empty oxygen hole polaron state in the middle of the valence band (VB) to conduction band (CB) energy gap. The onsite Coulomb interaction pushes the defect state into the middle of the gap as opposed to an unoccupied continuum state at the top of the valence band. With standard DFT the empty Cu 3d states lie just above the valence band edge, while with the + U correction on the Cu 3d states there is clear shift of these states into the energy gap. Examining the position of the empty Cu 3d states, one could conclude that the TiO_2 energy gap could be reduced by up to 0.5 eV upon Cu doping.

The charge compensation mechanism for doping of TiO_2 with lower valance cation dopants is the formation of oxygen vacancies. Therefore, given the 2+ oxidation state of Cu, one neutral oxygen species per Cu is removed from different sites in Cu-doped rutile and anatase. The most stable site for a compensating oxygen vacancy was determined and apical and equatorial oxygen sites neighbouring the dopant are the most stable, with vacancy formation energies of 0.46 (0.16) eV and 0.02 (−0.40) eV in rutile (anatase). Both oxygen sites show either negative or small, positive formation energies showing that oxygen vacancy formation is the charge compensation mechanism in Cu-doped TiO_2. This trend corroborates that found in a previous study of the effect of oxygen vacancies on the magnetic moment of Cu-doped rutile TiO_2 [51].

Fig. 6 shows the geometry of the charge compensated structures of Cu-doped TiO_2. For rutile and anatase the copper dopant and two neighbouring titanium ions each coordinate to five oxygen ions. This under-coordination leads to a distortion, with the titanium ions moving off their lattice sites and outwards from the vacancy site along the direction of the missing bond. This distortion is accompanied by a shortened Ti−O bond to the oxygen ion positioned opposite the vacancy. For rutile, this shortened bond is 1.84 Å compared to 2.02 Å for equivalent bonds away from the vacancy site. In anatase, the Ti-O distances are shortened by up to 0.15 Å. The oxygen vacancy has little effect on the remaining Cu−O bonds.

Fig. 6 also shows the excess spin density plots and the associated PEDOS for the compensating oxygen vacancy. The same trend is exhibited in the excess spin density plots of both rutile (Fig. 6(a)) and anatase (Fig. 6(b)) in that the excess spin is localized on the Cu dopant. The small spin on four neighbouring oxygen ions arises from covalency in the Cu−O bonds. The fifth oxygen, in both cases, is that positioned at an equatorial site opposite the vacancy. The computed Bader charges for Cu are 9.7 and 9.8 electrons for rutile and anatase, consistent with a Cu^{2+} oxidation state, which is unaffected by the charge compensation process.

For both TiO_2 polymorphs, the PEDOS plots are significantly altered upon forming the compensating vacancy. The EDOS displays a peak attributed to the empty 3d orbital of the Cu^{2+} oxidation state. For rutile, this peak lies in the gap just below the CB minimum whereas for anatase this peak coincides with the bottom of the CB. For both polymorphs, the charge compensating vacancy thus shifts the Cu 3d states closer to the CB edge of TiO_2. Around the valance band region, Cu-doped anatase shows a filled Cu 3d state above the TiO_2 valence band edge, while for rutile, this state lies below the valence band edge. The empty oxygen hole states disappear after charge compensation, as expected.

Thus, a small reduction in the band gap at this Cu doping concentration is proposed for rutile and anatase. For rutile, the shift is 0.3 eV and for anatase the proposed band gap decrease is 0.2 eV. Since these results should be regarded with caution given that this DFT + U set-up is not quantitatively describing the band gap of TiO_2, we ran single point hybrid DFT calculations of Cu-doped TiO_2. These use the HSE06 functional, with 25% Fock exchange and a screening parameter of 0.2 $Å^{-1}$. The PEDOS in Fig. 7 for doped anatase shows similar trends as the DFT + U result, despite the differences in the DFT + U and hybrid DFT energy gaps. With no charge compensating oxygen vacancy, the position of Cu 3d and O 2p polaron states are similar to those from DFT + U. With the charge compensating vacancy, the occupied Cu 3d states are similar to those found with DFT + U but the empty Cu 3d states lie above the TiO_2 conduction band edge. This gives a band gap reduction of 0.2 eV, similar to DFT + U. Thus, both DFT approaches appear to suggest that doping with Cu induces only a small, if any, red shift in light absorption.

Finally, the formation of a neutral oxygen vacancy in charge compensated Cu-doped anatase has been studied. This is motivated by the experiments described previously, in which TiO_2 is calcined to over 500 °C, at which temperatures the formation of oxygen vacancy defects is likely. We compute a formation energy of 3.3 eV for the most stable oxygen vacancy site in charge compensated 3% Cu-doped anatase, with the atomic structure, spin density and PEDOS shown in Fig. 6(c). Given the elevated temperatures in the experiments, such reducing oxygen vacancies will be present and we can examine the effect of these vacancies on the electronic properties of Cu-doped anatase. We note that the computed oxygen vacancy formation energy of Cu-doped anatase is lower than that of undoped anatase, which is 4.92 eV in our DFT + U set-up. This would promote the formation of oxygen vacancies which would then lower the temperature at which the phase transition takes place. However, we find that as the concentration of oxygen vacancies increases the computed formation energy for Cu-doped anatase increases from 3.3 eV to 3.6 eV for a third vacancy. We can conclude that the mechanism that underpins the experimental observation that the anatase phase persists to higher temperatures with Cu doping cannot be fully accounted for by the thermodynamics of simple oxygen vacancy formation. It is possible the sulfate in the copper precursor also contributes to inhibiting the phase transformation [59].

The computed Bader charge on Cu is 10.4 electrons, with a spin of 0.1 μ_B, which is consistent with reduction to Cu^{1+}. One Ti cation has a Bader charge of 10.5 electrons and a spin of 0.95 μ_B, which is consistent with a Ti^{3+} cation (all other Ti cations are Ti^{4+} with computed Bader charges of 9.6 electrons). The formation of a neutral oxygen vacancy thus reduces one Ti cation to Ti^{3+} and the Cu dopant to Cu^{1+}. Comparing with the XPS data, this is consistent with the assignment of reduced Cu^{1+} at elevated temperatures. The decrease in peak intensities of the Cu^{2+} satellites with increasing temperature is also consistent with Cu^{2+} reduction by oxygen vacancy formation. Finally, the PEDOS in Fig. 6(c) shows the introduction of occupied Cu^{1+} states

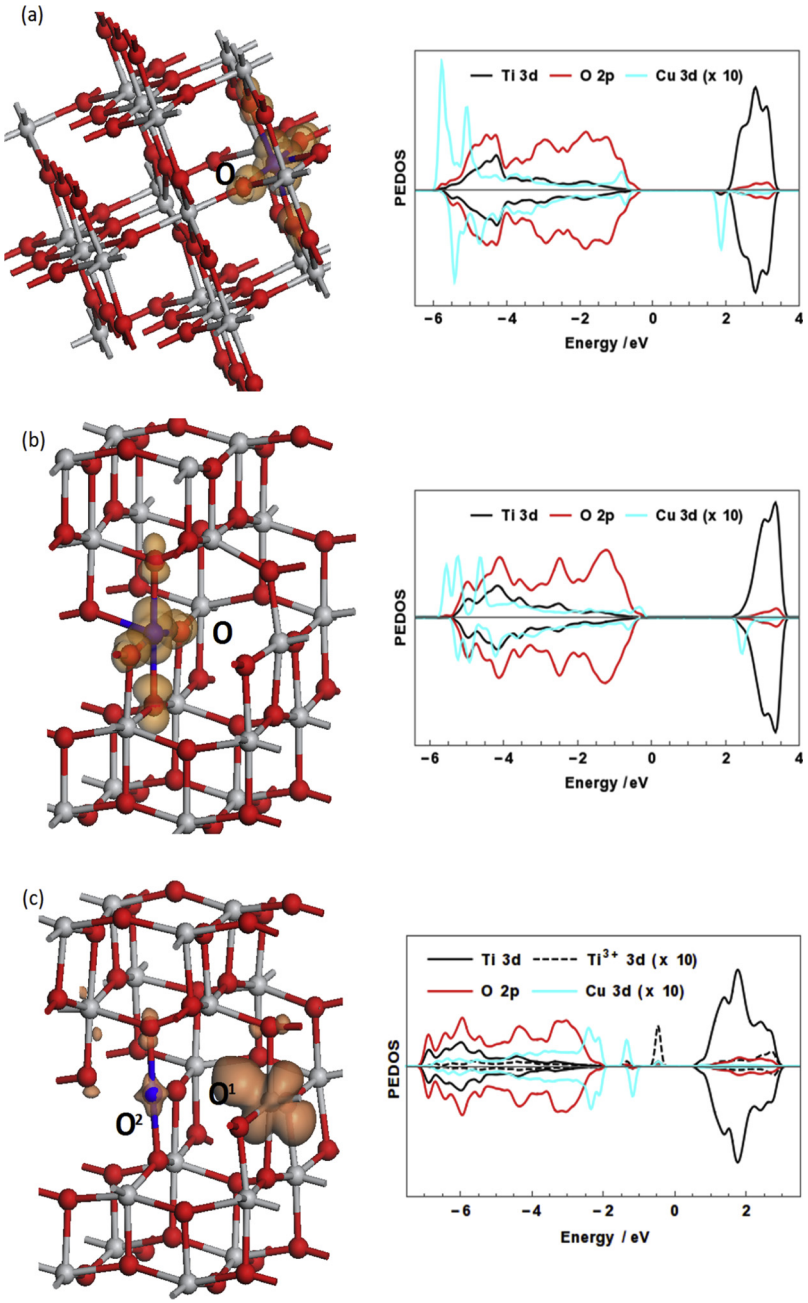

Fig. 6. Excess spin density and PEDOS plots of charge compensated Cu-doped (a) rutile and (b) anatase TiO_2. Cu is represented by a blue sphere and the black circle marks the location of the charge compensating oxygen vacancy. (c) Cu-doped anatase with a second, reducing oxygen vacancy, where O^1 and O^2 indicate the site of the compensating and reducing oxygen vacancies. The spin density isosurface is set to 0.02 electrons $Å^{-3}$ (For interpretation of the references to colour in this figure legend, the reader is referred to the web version of this article).

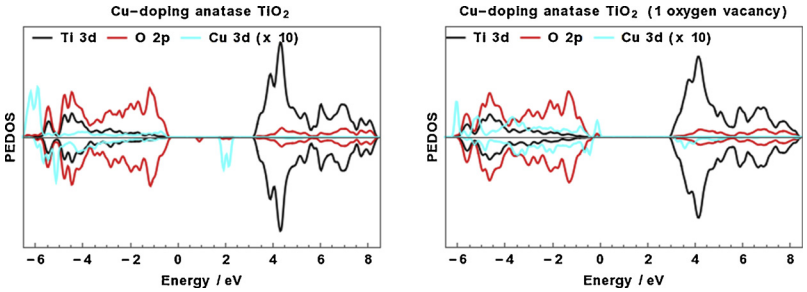

Fig. 7. Hybrid DFT PEDOS for Cu-doped TiO_2. Left panel: Cu-doped anatase with no compensating oxygen vacancy, right panel: Cu-doped anatase with the compensating oxygen vacancy.

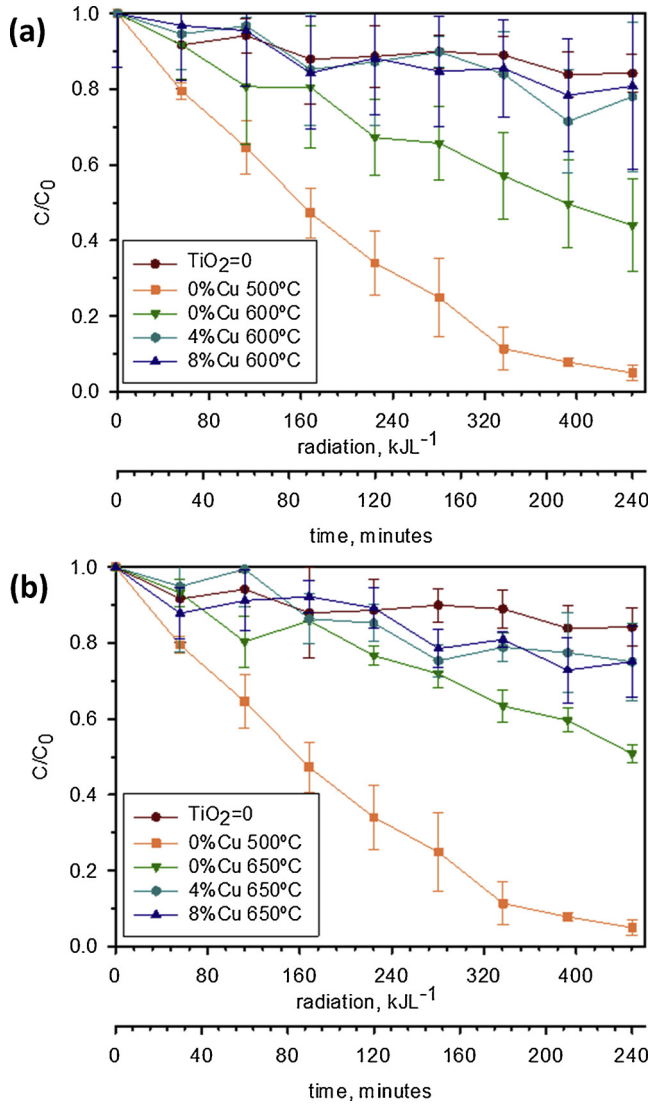

Fig. 8. Degradation of 1,4-dioxane by Cu-doped TiO_2 photocatalysis at (a) 600 °C and (b) 650 °C compared with TiO_2 prepared at 500 °C and radiation without catalyst.

in the TiO_2 valence-conduction band energy gap. These states can enhance charge recombination after excitation that could result in reduced photocatalytic activity; this is discussed in the following section.

3.7. Photocatalytic analysis

The adsorption of 1,4-dioxane onto the Cu-doped TiO_2 catalyst surface did not exceed 10% in the dark control experiments, where the catalyst was added without applying solar light; as well as in the control trials applying radiation without adding the catalyst (Fig. 8). Here we examined samples with all Cu concentrations and calcined at 600 °C & 650 °C.

The highest degradation of 1,4-dioxane was achieved by adding TiO_2 prepared at 500 °C without Cu doping. With this sample, the majority of the 1,4-dioxane was degraded within 240 min. Increasing the temperature to 600 or 650 °C limited the extent of 1,4-dioxane degradation (Figs. 8, S7 and S8). The inclusion of Cu does not, therefore, result in any improvement of the photocatalytic activity of TiO_2 (Figs. 8, S8 and S9). This is also irrespective of the polymorph of TiO_2 present as a result of Cu-doping and calcination temperature. Thus, while Cu doping can be used to enhance the stability of anatase TiO_2 to higher temperatures, and give a higher anatase content, the incorporation of Cu has the effect of reducing photocatalytic activity towards dioxane removal.

This behaviour agrees with previous studies, in which Cu-doping did not always report an improvement of the photocatalytic efficiency of Cu-TiO_2 even in the anatase phase [9,22,23]. This is usually attributed to the recombination of electron-hole pairs at defect centres. This process is favoured by the presence of Cu within the TiO_2 catalyst; as well as to the prevention of photon absorption by TiO_2 due to the presence of Cu [23]. Moreover, Colon et al. [22] reported that deactivation may be caused by the formation of CuO species at the surface of the catalyst [22]. Cu^{2+}, identified by XPS in TiO_2 calcined at 600 and 650 °C, would impact on photocatalytic activity through migration of a photogenerated electron from the conduction band of TiO_2, which prevents the generation of $OH^{\cdot}$ [22]. In addition, Lopes et al. reported higher activity of the catalysts with the lowest copper content due to a higher Cu(I)/Cu(0) ratio [22].

In contrast to this study, a number of studies have found an increase of photocatalytic activity when using copper nitrate as the copper precursor [9,24–28]. For example, López et al. (2009) found that the photodegradation of dichlorophenoxyacetic acid was enhanced with the inclusion of copper, compared with bare titania. They concluded that the increased photocatalytic activity was due to the stabilisation of Cu^{1+} by TiO_2 [9]. Another example is the study by Fisher et al. [25] in which the effect of copper doping (with a copper nitrate precursor) and Cu-N co-doping on TiO_2 were explored. These authors found that there was improved activity for all doped samples compared to bare titania when examining the photocatalytic degradation of methylene blue and the inactivation of microbiological materials [25].

4. Conclusions

Cu-doped TiO_2 was synthesised using a modified sol-gel method to explore the effect of Cu-doping of anatase TiO_2 on the transition to rutile at elevated temperatures. Samples were calcined between 500 and 800 °C. We find that in comparison to the control (0% Cu) the copper doped samples improve the stabilisation of anatase at elevated temperatures, thus shifting the transition temperature higher. Doping with 8% Cu was found to be optimum. At 600 °C, the control sample (with 0% Cu) contained 34.3% anatase while at the same temperature; all doped samples were 100% anatase. At 650 °C, the 4% and 8% Cu-TiO_2 had anatase contents of 27.3% and 74.3% respectively. All samples heated to 700 °C were 100% rutile. XPS showed no indication of Ti-Cu binding, only Ti-O binding was present. XPS was also used for determining that the increase in temperature resulted in copper being reduced from Cu^{2+} to Cu^{1+}.

The doping of bulk rutile and anatase TiO_2 with Cu was investigated using different DFT approaches. We have shown that charge compensating oxygen vacancies form to balance the lower +2 oxidation state of Cu. The density of states shows localised peaks near the valence and conduction band edges, arising from the empty Cu 3d state of Cu^{2+}. These result in a predicted small red shift in the adsorption edge. Computed formation energies for the formation of the reducing oxygen vacancy are lower compared to undoped anatase, although the energy cost increases with vacancy concentration. Thus, the increases in the temperature for the transition from anatase to rutile is most likely not solely due to oxygen vacancy formation, with sulfate from the copper precursor potentially playing a role. Formation of reducing oxygen vacancies reduces Cu^{2+} to Cu^{1+} and Ti^{4+} to Ti^{3+} with a localised Cu-derived gap state that can act as a recombination centre and degrade the photocatalytic activity of anatase.

Photocatalysis studies, using 1,4-dioxane, indicated that inclusion of copper induced a significant reduction in the rate of photodegradation. The sample that showed the most photocatalytic activity was the 0% Cu-TiO_2 (100% anatase), which showed a 1,4-dioxane removal of approx. 90% after 450 kJ L^{-1} (240 min). All copper doped samples showed 1,4-dioxane removal of between 20–40% over the same time

and radiation. When we compare these findings to the results from the DFT studies, we suggest that the reduction in activity over undoped TiO_2 most likely arises from the presence of the Cu^{1+}/Cu^{2+}-induced defect states described in Section 3.6 which act as traps for charges and thus promote recombination.

Acknowledgements

SR and MN acknowledge support from Science Foundation Ireland (SFI) through the US-Ireland R&D Partnership Program, grant number SFI 14/US/E2915, the ERA.Net for Materials Research and Innovation (M-ERA.Net 2), Horizon 2020 grant agreement number 685451, SFI Grant Number SFI/16/M-ERA/3418 (RATOCAT) and the European Commission through the COST Action CM1104 “Reducible Metal Oxides, Structure and Function”. We acknowledge access to computing resources at Tyndall provided by SFI and by the SFI and Higher Education Authority funded Irish Centre for High End Computing. CB, LM and SP would like to acknowledge access to Raman Spectroscopy at Centre for Research in Engineering Surface Technology (CREST), FOCAS Institute, Dublin Institute of Technology, Kevin Street. CB & PG would like to acknowledge the Institute of Technology Sligo President’s Bursary for providing financial support. SP is grateful to the Renewable Engine project funded by European Union’s INTERREG VA Programme, managed by the Special EU Programmes Body (SEUPB), with match funding provided by the Department for the Economy and Department of Jobs, Enterprise and Innovation in Ireland. DH would like to acknowledgment the Universidad de Valladolid for granting the stay at the Institute of Technology Sligo. DH would also to thank Ministerio de Economía y Competitividad of Spain (research grant number: CTM2016-77948-R) for providing research funding.

Appendix A. Supplementary data

Supplementary material related to this article can be found, in the online version, at doi:https://doi.org/10.1016/j.apcatb.2019.01.058.

References

[1] A. Fujishima, K. Honda, Electrochemical photolysis of water at a semiconductor electrode, Nature 238 (1972) 37.
[2] M. Ni, M.K. Leung, D.Y. Leung, K. Sumathy, A review and recent developments in photocatalytic water-splitting using TiO2 for hydrogen production, Renew. Sustain. Energy Rev. 11 (2007) 401–425.
[3] B. Ohtani, Preparing articles on photocatalysis—beyond the illusions, misconceptions, and speculation, Chem. Lett. 37 (2008) 216–229.
[4] B. Ohtani, Photocatalysis A to Z—what we know and what we do not know in a scientific sense, J. Photochem. Photobiol. C Photochem. Rev. 11 (2010) 157–178.
[5] D.A. Hanaor, C.C. Sorrell, Review of the anatase to rutile phase transformation, J. Mater. Sci. 46 (2011) 855–874.
[6] W.-K. Wang, J.-J. Chen, X. Zhang, Y.-X. Huang, W.-W. Li, H.-Q. Yu, Self-induced synthesis of phase-junction TiO2 with a tailored rutile to anatase ratio below phase transition temperature, Sci. Rep. 6 (2016) 20491.
[7] A. Okasha, F. Gomaa, H. Elhaes, M. Morsy, S. El-Khodary, A. Fakhry, M. Ibrahim, Spectroscopic analyses of the photocatalytic behavior of nano titanium dioxide, Spectrochim. Acta A. Mol. Biomol. Spectrosc. 136 (2015) 504–509.
[8] Y. Boyjoo, H. Sun, J. Liu, V.K. Pareek, S. Wang, A review on photocatalysis for air treatment: from catalyst development to reactor design, Chem. Eng. J. 310 (2017) 537–559.
[9] R. López, R. Gómez, M.E. Llanos, Photophysical and photocatalytic properties of nanosized copper-doped titania sol–gel catalysts, Catal. Today 148 (2009) 103–108.
[10] S. Mathew, P. Ganguly, S. Rhatigan, V. Kumaravel, C. Byrne, S. Hinder, J. Bartlett, M. Nolan, S. Pillai, Cu-doped TiO2: visible light assisted photocatalytic antimicrobial activity, Appl. Sci. 8 (2018) 2067.
[11] P. Periyat, S.C. Pillai, D.E. McCormack, J. Colreavy, S.J. Hinder, Improved high-temperature stability and sun-light-driven photocatalytic activity of sulfur-doped anatase TiO2, J. Phys. Chem. C 112 (2008) 7644–7652.
[12] V. Etacheri, M.K. Seery, S.J. Hinder, S.C. Pillai, Oxygen rich titania: a dopant free, high temperature stable, and visible-light active anatase photocatalyst, Adv. Funct. Mater. 21 (2011) 3744–3752.
[13] R. Fagan, D.E. McCormack, D.D. Dionysiou, S.C. Pillai, A review of solar and visible light active TiO 2 photocatalysis for treating bacteria, cyanotoxins and contaminants of emerging concern, Mater. Sci. Semicond. Process. (2015).
[14] C. Byrne, R. Fagan, S. Hinder, D.E. McCormack, S.C. Pillai, New approach of modifying the anatase to rutile transition temperature in TiO 2 photocatalysts, RSC Adv. 6 (2016) 95232–95238.
[15] F.E. Oropeza, J. Harmer, R. Egdell, R.G. Palgrave, A critical evaluation of the mode of incorporation of nitrogen in doped anatase photocatalysts, J. Chem. Soc. Faraday Trans. 12 (2010) 960–969.
[16] X. Fang, Z. Zhang, Q. Chen, H. Ji, X. Gao, Dependence of nitrogen doping on TiO 2 precursor annealed under NH 3 flow, J. Solid State Chem. 180 (2007) 1325–1332.
[17] R. Janes, L. Knightley, C. Harding, Structural and spectroscopic studies of iron (III) doped titania powders prepared by sol-gel synthesis and hydrothermal processing, Dye. Pigment. 62 (2004) 199–212.
[18] H.M. Yadav, S.V. Otari, V.B. Koli, S.S. Mali, C.K. Hong, S.H. Pawar, S.D. Delekar, Preparation and characterization of copper-doped anatase TiO 2 nanoparticles with visible light photocatalytic antibacterial activity, J. Photochem. Photobiol. A: Chem. 280 (2014) 32–38.
[19] L. Kőrösi, S. Papp, J. Ménesi, E. Illés, V. Zöllmer, A. Richardt, I. Dékány, Photocatalytic activity of silver-modified titanium dioxide at solid–liquid and solid–gas interfaces, Colloids Surf. A Physicochem. Eng. Asp. 319 (2008) 136–142.
[20] N.T. Nolan, M.K. Seery, S.J. Hinder, L.F. Healy, S.C. Pillai, A systematic study of the effect of silver on the chelation of formic acid to a titanium precursor and the resulting effect on the anatase to rutile transformation of TiO2, J. Phys. Chem. C 114 (2010) 13026–13034.
[21] T. Theivasanthi, M. Alagar, X-Ray Diffraction Studies of Copper Nanopowder, arXiv preprint arXiv:1003.6068 (2010).
[22] G. Colón, M. Maicu, M.C. Hidalgo, J.A. Navío, Cu-doped TiO2 systems with improved photocatalytic activity, Appl. Catal. B 67 (2006) 41–51.
[23] R.S. Wong, J. Feng, X. Hu, P.L. Yue, Discoloration and mineralization of non-biodegradable azo dye orange II by copper-doped TiO2 nanocatalysts, J. Environ. Sci. Health, Part A 39 (2004) 2583–2595.
[24] L. Yoong, F.K. Chong, B.K. Dutta, Development of copper-doped TiO 2 photocatalyst for hydrogen production under visible light, Energy 34 (2009) 1652–1661.
[25] M.B. Fisher, D.A. Keane, P. Fernandez-Ibanez, J. Colreavy, S.J. Hinder, K.G. McGuigan, S.C. Pillai, Nitrogen and copper doped solar light active TiO 2 photocatalysts for water decontamination, Appl. Catal. B 130 (2013) 8–13.
[26] K. Lalitha, G. Sadanandam, V.D. Kumari, M. Subrahmanyam, B. Sreedhar, N.Y. Hebalkar, Highly stabilized and finely dispersed Cu2O/TiO2: a promising visible sensitive photocatalyst for continuous production of hydrogen from glycerol: water mixtures, J. Phys. Chem. C 114 (2010) 22181–22189.
[27] M.M. Momeni, Y. Ghayeb, Z. Ghonchegi, Fabrication and characterization of copper doped TiO 2 nanotube arrays by in situ electrochemical method as efficient visible-light photocatalyst, Ceram. Int. 41 (2015) 8735–8741.
[28] H. Nishikiori, T. Sato, S. Kubota, N. Tanaka, Y. Shimizu, T. Fujii, Preparation of Cu-doped TiO2 via refluxing of alkoxide solution and its photocatalytic properties, Res. Chem. Intermed. 38 (2012) 595–613.
[29] L. Yoong, F.K. Chong, B.K. Dutta, Development of copper-doped TiO2 photocatalyst for hydrogen production under visible light, Energy 34 (2009) 1652–1661.
[30] R.A. Spurr, H. Myers, Quantitative analysis of anatase-rutile mixtures with an X-ray diffractometer, Anal. Chem. 29 (1957) 760–762.
[31] P. Scherrer, Bestimmung der Grösse und der inneren Struktur von Kolloidteilchen mittels Röntgenstrahlen, Nachrichten von der Gesellschaft der Wissenschaften zu Göttingen, Mathematisch-physikalische Klasse 1918 (1918) 98–100.
[32] G. Kresse, J. Furthmüller, Efficiency of ab-initio total energy calculations for metals and semiconductors using a plane-wave basis set, Comput. Mater. Sci. 6 (1996) 15–50.
[33] G. Kresse, J. Furthmüller, Efficient iterative schemes for ab-initio total-energy calculations using a plane-wave basis set, Phys. Rev. B 54 (1996) 11169.
[34] G. Kresse, D. Joubert, From ultrasoft pseudopotentials to the projector augmented-wave method, Phys. Rev. B 59 (1999) 1758–1775.
[35] P.E. Blöchl, Projector augmented-wave method, Phys. Rev. B 50 (1994) 17953–17979.
[36] L.S. Yoong, F.K. Chong, B.K. Dutta, Development of copper-doped TiO2 photocatalyst for hydrogen production under visible light, Energy 34 (2009) 1652–1661.
[37] R. Chand, E. Obuchi, K. Katoh, H.N. Luitel, K. Nakano, Enhanced photocatalytic activity of TiO2/SiO2 by the influence of Cu-doping under reducing calcination atmosphere, Catal. Commun. 13 (2011) 49–53.
[38] M. Nolan, G.W. Watson, Hole localization in Al doped silica: a DFT + U description, J. Chem. Phys. 125 (2006) 144701.
[39] M. Nolan, G.W. Watson, The electronic structure of alkali doped alkaline earth metal oxides: Li doping of MgO studied with DFT-GGA and GGA + U, Surf. Sci. 586 (2005) 25–37.
[40] J.J. Carey, M. Nolan, Dissociative adsorption of methane on the Cu and Zn doped (111) surface of CeO2, Appl. Catal. B 197 (2016) 324–336.
[41] M. Nolan, S.D. Elliott, The p-type conduction mechanism in Cu2O: a first principles study, Phys. Chem. Chem. Phys. 8 (2006) 5350–5358.
[42] B.J. Morgan, G.W. Watson, A DFT + U description of oxygen vacancies at the TiO2 rutile (1 1 0) surface, Surf. Sci. 601 (2007) 5034–5041.
[43] M. Nolan, S.D. Elliott, J.S. Mulley, R.A. Bennett, M. Basham, P. Mulheran, Electronic structure of point defects in controlled self-doping of the ${\text{TiO}}_{2}$ (110) surface: combined photoemission spectroscopy and density functional theory study, Phys. Rev. B 77 (2008) 235424.
[44] P.M. Kowalski, M.F. Camellone, N.N. Nair, B. Meyer, D. Marx, Charge localization dynamics induced by oxygen vacancies on the ${\mathrm{TiO}}_{2}(110)$ surface, Phys. Rev. Lett. 105 (2010) 146405.
[45] G. Henkelman, A. Arnaldsson, H. Jónsson, A fast and robust algorithm for Bader decomposition of charge density, Comput. Mater. Sci. 36 (2006) 354–360.
[46] V. Etacheri, M.K. Seery, S.J. Hinder, S.C. Pillai, Highly visible light active TiO2 − x N x heterojunction photocatalysts, Chem. Mater. 22 (2010) 3843–3853.
[47] R.V. Siriwardane, J.A. Poston Jr, E.P. Fisher, M.-S. Shen, A.L. Miltz, Decomposition

of the sulfates of copper, iron (II), iron (III), nickel, and zinc: XPS, SEM, DRIFTS, XRD, and TGA study, Appl. Surf. Sci. 152 (1999) 219–236.
[48] J. Yang, H. Bai, X. Tan, J. Lian, IR and XPS investigation of visible-light photocatalysis—nitrogen–carbon-doped TiO 2 film, Appl. Surf. Sci. 253 (2006) 1988–1994.
[49] H. Gao, G. Wang, Y. Luan, K. Chaikittikul, X. Zhang, M. Yang, W. Dong, Z. Shi, A fast synthesis of hierarchical yolk–shell copper hydroxysulfates at room temperature with adjustable sizes, CrystEngComm 16 (2014) 2520–2526.
[50] Y. Liu, P. Bailey, T.C. Noakes, G.E. Thompson, P. Skeldon, M.R. Alexander, Chemical environment of copper at the surface of a CuAl2 model alloy: XPS, MEIS and TEM analyses, Surf. Interface Anal. 36 (2004) 339–346.
[51] S. Duhalde, M.F. Vignolo, F. Golmar, C. Chiliotte, C.E.R. Torres, L.A. Errico, A.F. Cabrera, M. Rentería, F.H. Sánchez, M. Weissmann, Appearance of room-temperature ferromagnetism in Cu-doped ${\mathrm{TiO}}_{2\ensuremath{-}\ensuremath{\delta}}$ films, Phys. Rev. B 72 (2005) 161313.
[52] A. Iwaszuk, M. Nolan, Charge compensation in trivalent cation doped bulk rutile TiO 2, J. Phys. Condens. Matter. 23 (2011) 334207.
[53] M.-H. Du, S.B. Zhang, Impurity-bound small polarons in ZnO: hybrid density functional calculations, Phys. Rev. B 80 (2009) 115217.
[54] D.O. Scanlon, A. Walsh, B.J. Morgan, M. Nolan, J. Fearon, G.W. Watson, Surface sensitivity in lithium-doping of MgO: a density functional theory study with correction for on-site Coulomb interactions, J. Phys. Chem. C 111 (2007) 7971–7979.
[55] O.F. Schirmer, O − bound small polarons in oxide materials, J. Phys. Condens. Matter 18 (2006) R667.
[56] A.M. Stoneham, J. Gavartin, A.L. Shluger, A.V. Kimmel, D.M. Ramo, H.M. Rønnow, G. Aeppli, C. Renner, Trapping, self-trapping and the polaron family, J. Phys. Condens. Matter 19 (2007) 255208.
[57] Y. Maimaiti, M. Nolan, S.D. Elliott, Reduction mechanisms of the CuO(111) surface through surface oxygen vacancy formation and hydrogen adsorption, Phys. Chem. Chem. Phys. 16 (2014) 3036–3046.
[58] H. Zhang, X. Yu, J.A. McLeod, X. Sun, First-principles study of Cu-doping and oxygen vacancy effects on TiO2 for water splitting, Chem. Phys. Lett. 612 (2014) 106–110.
[59] S.R. Yoganarasimhan, C.N.R. Rao, Mechanism of crystal structure transformations. Part 3. —Factors affecting the anatase-rutile transformation, Trans. Faraday Soc. 58 (1962) 1579–1589.